Formation of unconventional standing waves at graphene edges by valley mixing and pseudospin rotation

Changwon Park[a], Heejun Yang[b], Andrew J. Mayne[c], Gérald Dujardin[c], Sunae Seo[d], Young Kuk[a], Jisoon Ihm[a,1], and Gunn Kim[d,1]

[a]Department of Physics and Astronomy, Seoul National University, Seoul 151-747, Korea; [b]Graphene Research Center, Samsung Advanced Institute of Technology, Samsung Electronics, Yongin, Gyeonggi-do 446-712, Korea; [c]Institut des Sciences Moléculaires d'Orsay, Centre National de la Recherche Scientifique, Bât. 210, Univ Paris Sud, 91405 Orsay, France; and [d]Department of Physics and Graphene Research Institute, Sejong University, Seoul 143-747, Korea

Contributed by Jisoon Ihm, September 14, 2011 (sent for review June 8, 2011)

We investigate the roles of the pseudospin and the valley degeneracy in electron scattering at graphene edges. It is found that they are strongly correlated with charge density modulations of short-wavelength oscillations and slowly decaying beat patterns in the electronic density profile. Theoretical analyses using nearest-neighbor tight-binding methods and first-principles density-functional theory calculations agree well with our experimental data from scanning tunneling microscopy. The armchair edge shows almost perfect intervalley scattering with pseudospin invariance regardless of the presence of the hydrogen atom at the edge, whereas the zigzag edge only allows for intravalley scattering with the change in the pseudospin orientation. The effect of structural defects at the graphene edges is also discussed.

In graphene, the pseudospin and the valley flavor arise as new types of quantum degrees of freedom due to the honeycomb lattice comprising two sublattices (A and B) and two inequivalent Dirac points (K and K') in the Brillouin zone, respectively. Unique electronic properties of graphene result in striking phenomena such as Klein tunneling (1, 2), Veselago lens (3), and valley-polarized currents (4). A variety of edge properties (5–8) of graphene and graphene nanoribbons (9) have been investigated and interference images using the scanning tunneling microscopy (STM) were also reported before (10). However, electron scattering behaviors at graphene edges have not been well understood yet.

A conventional metal with a terrace and a step can be modeled as a two-dimensional (2D) free electron gas with a hard wall and the standing wave formed at the edge can be analytically solved. This behavior was directly observed at the steps of Au(111) and Cu(111) surfaces by STM (11–13). Now, a question arises as to whether the graphene edge has a similar standing wave pattern to conventional metals, and how two sublattices and two inequivalent valleys in graphene affect the scattering and the standing wave formation. In this article, we report the STM topographic image at the graphene edge and show that the interference pattern observed there is quantitatively understood in terms of intra- and intervalley scattering processes and that the pseudospin exhibits characteristic behaviors, depending on the edge configuration.

Results and Discussion

Due to the crystal momentum conservation along the edge, available backscattering channels are limited to the Bloch states of the same wavevector component in the edge direction (k_y) as the incident wave. To describe the conservation of k_y (and the nonconservation of k_x) most conveniently, we choose the rectangular Brillouin zone (equivalent to the hexagonal first Brillouin zone) in the armchair or the zigzag edge case, as depicted in Fig. 1 A or B, and mark two distinct Fermi circles (of the doped graphene) around K and K' valleys on the Brillouin zone. Green arrows represent the orientations of the pseudospin, namely, the two-component cell-periodic part of the Bloch wavefunction. (However, one should be cautious about the fact that the orientation of the pseudospin can change according to the choice of the relative phase of the basis functions.) For a given wavevector k_y, there are two intersecting points for each Fermi circle, corresponding to left and right propagating states. Fig. 1 C and D show two possible (intravalley and intervalley) backscattering channels at the armchair edge, whereas only one intravalley scattering channel is allowed at the zigzag edge (14). In the nearest-neighbor tight-binding method, the scattering waves at graphene edges are uniquely determined by boundary matching conditions. As shown in the left boxes of Fig. 2, we chose three representative model structures (15) for the armchair edge that were observed in the transmission electron microscopy image (7), as well as another structure of the zigzag edge. The resulting reflection probabilities and electronic density profiles were calculated with appropriate hopping parameters from the first-principles Wannier function analysis and the Fermi energy (E_F) was chosen to be 0.3 eV above the Dirac point (E_D). Note that the epitaxial graphene on the SiC(0001) surface is n-doped and typically $E_F - E_D \approx 0.3 - 0.4$ eV (16).

Considering the crystal momentum conservation at the armchair edge, intervalley and intravalley scatterings can in principle be allowed as mentioned above (Fig. 1C). However, when the boundary matching conditions are applied, the actual scattering at the ideal armchair edge is an almost entirely intervalley process for all incident angles (17, 18), and the pseudospin of the incident wave is identical to that of the scattering wave as can be inferred from Fig. 1A. In other words, the pseudospin is invariant throughout the scattering process at the ideal armchair edge. By integrating all scattering waves on the Fermi surface, we construct a laterally averaged electronic density profile in real space (in the right box of Fig. 2). For the armchair edge, the electronic density profile can be written as

$$\int_{-\frac{\pi}{2}}^{\frac{\pi}{2}} (|\psi_K^{\theta,\mathrm{in}}(x) + \psi_{K'}^{\theta,\mathrm{out}}(x)|^2 + |\psi_{K'}^{\theta,\mathrm{in}}(x) + \psi_K^{\theta,\mathrm{out}}(x)|^2) d\theta \propto 1 - \cos(K_0 x) J_0(2k_R x), \quad [1]$$

where x is the distance from the edge, $\psi_{K(K')}^{\theta,\mathrm{in(out)}}(x)$ is the incident (scattering) planewave on the $K(K')$-valley Fermi surface with the angle θ, K_0 the length of $\overline{\Gamma K}$ in k-space, k_R the radius of the

Author contributions: C.P., S.S., Y.K., J.I., and G.K. designed research; C.P., H.Y., A.J.M., G.D., Y.K., J.I., and G.K. performed research; C.P., H.Y., and G.K. analyzed data; and C.P., H.Y., J.I., and G.K. wrote the paper.

The authors declare no conflict of interest.

[1]To whom correspondence may be addressed. E-mail: jihm@snu.ac.kr or gunnkim@sejong.ac.kr.

This article contains supporting information online at www.pnas.org/lookup/suppl/doi:10.1073/pnas.1114548108/-/DCSupplemental.

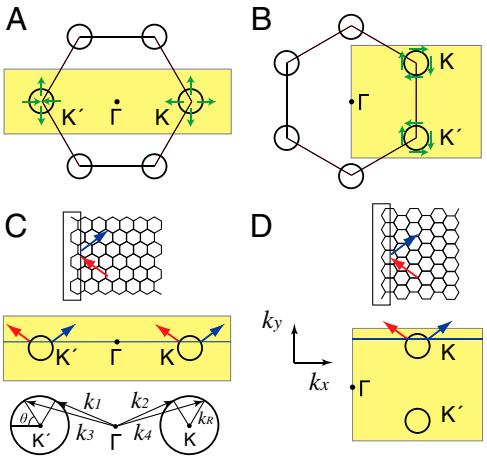

Fig. 1. Schematic Fermi surfaces and pseudospin fields of (*A*) the armchair edge and (*B*) the zigzag edge. The Brillouin zone is transformed to a rectangle in each case, for convenience in taking into account the symmetry (translation symmetry in the *y*-direction and the broken symmetry in the *x*-direction) by the presence of the edge. Green arrows stand for the orientations of the pseudospin. Available scattering channels of a given incident wave are presented for (*C*) the armchair edge and (*D*) the zigzag edge. Red arrows indicate incident directions and blue arrows scattering directions, respectively. The size of the Fermi circle is exaggerated for visual clarity.

Fermi circle, and J_0 the zeroth-order Bessel function. Because the wavevectors are defined up to the reciprocal lattice vectors, we take the freedom of choosing the wavevectors so that the resulting wavevector difference (between K and K' valleys) in the above expression has the smallest magnitude.

Very interestingly, the armchair edge has intervalley scattering which is not shared by the 2D free electron gas. In the electronic density profile near the armchair edge, a short-period oscillation and a slowly decaying beat pattern are observed. First, a short-period oscillation comes from the intervalley scattering, and its wavelength is approximately 0.37 nm; i.e., $3a/2$ where a (=0.246 nm) is the length of the graphene lattice vector. Therefore, this phenomenon is a unique property of materials with multiple Fermi circles. Second, the slowly decaying oscillatory behavior has the same origin as the one observed on the terrace of the conventional metal (11). The characteristic period of the oscillation is a few nanometers. The Bessel-function-type envelope pattern is in general caused by quantum interference between incident and scattered electrons in 2D metals at the straight edge termination. Finally, a beat is an interference between two waves of slightly different wavevectors. As depicted in Fig. 1*C*, $|\vec{k}_2 - \vec{k}_1|$ (K to K' scattering) is slightly different from $|\vec{k}_3 - \vec{k}_4|$ (K' to K scattering), and these two intervalley scattering events result in the beat. Because the beat is associated with the radius of the Fermi circle (i.e., $|E_F| \neq |E_D|$), its period changes as the chemical potential (or the doping level) of graphene is altered.

According to our maximally localized Wannier function analysis, when there are no passivating atoms, the shortened C-C bond at the edge increases the hopping parameter. However, only slight changes in the proportion of two backscattering channels occur, and the electron density profile of the armchair edge with the dangling bonds (Fig. 2*B*) is almost indistinguishable from the hydrogen-passivated armchair edge (Fig. 2*A*). For the armchair edge with pentagons (Fig. 2*C*), both the intervalley and the intravalley scatterings take place for the obliquely incident wave because of different boundary matching conditions from the ideal edge, which means that the orientation of the pseudospin now changes. Although this mixing of intervalley and intravalley scattering channels modifies the charge modulation pattern, overall features of the electronic density profile in the right box of Fig. 2*C* looks similar to those of the hydrogen-passivated armchair edge. The armchair edge with pentagons also retains the node-like structure as in the ideal armchair edge. The reason is that the small-angle incident waves have large weights when forming a standing wave near the edge and are reflected dominantly via intervalley scattering for the armchair edge regardless of the details of the edge termination.

At the zigzag edge, on the other hand, only the intravalley scattering is allowed which shows a standing wave quite similar to the conventional metal surface. The electronic density profile of the zigzag edge is given by

$$\int_{-\frac{\pi}{2}}^{\frac{\pi}{2}} (|\psi_K^{\theta,\mathrm{in}}(x) + \psi_K^{\theta,\mathrm{out}}(x)|^2 + |\psi_{K'}^{\theta,\mathrm{in}}(x) + \psi_{K'}^{\theta,\mathrm{out}}(x)|^2) d\theta \propto 1 - J_0(2k_R x). \quad [2]$$

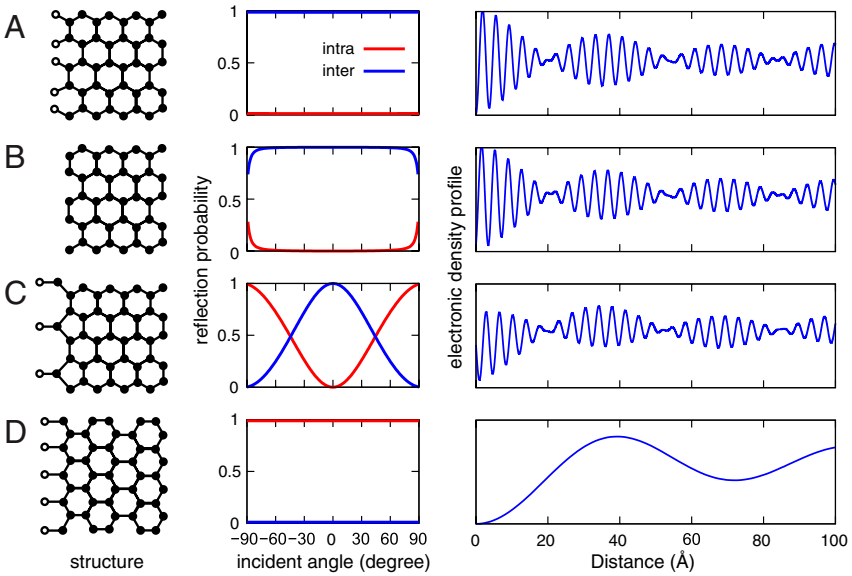

Fig. 2. For each structure (left boxes), the reflection probability of the K-valley-polarized wave (central box) and the laterally averaged electronic density profile from both valleys (right box) are shown (see [**1**] and [**2**] in the text). (*A*) is the armchair edge with hydrogen passivation, (*B*) the armchair edge without passivation, (*C*) the armchair edge with pentagons, and (*D*) the zigzag edge with hydrogen passivation, respectively. The Bloch cell-periodic part is ignored for clarity. In (*D*), the contribution of the localized edge eigenstates, existing only at the zigzag edge, is not included in the electronic density profile.

To reveal the characteristic feature of the scattering unambiguously, the contributions of edge states at the zigzag edge are not included in the electronic density profile. With the intravalley scattering at the zigzag edge, the pseudospin changes its orientation. Because the scattering is confined to the same valley, the pseudospin follows the change of the crystal momentum by scattering. This behavior shows sharp contrast to the pseudospin conservation at the armchair edge discussed above.

For a low-energy scattering, the diameter of the Fermi circle in graphene is small. Specifically, the Fermi circle diameter of slightly n-doped epitaxial graphene on the SiC(0001) surface is about 0.1 $Å^{-1}$ so that the intravalley scattering makes a long-period charge modulation pattern of a characteristic period of ~3 nm. Fig. 3*A* shows a real-space topographic image and a Fourier-filtered line profile of the experimental STM data of the armchair edge. In order to separate the beat and the Moiré pattern originating from the $6\sqrt{3}\times 6\sqrt{3}R30°$ periodicity of the SiC (0001) surface with a graphene layer, we used Fourier filtering to the STM topographic image (19). Although the period of the Moiré pattern and the beat are similar, their Fourier components are located at different positions in the reciprocal space and are distinguishable. By excluding components corresponding to the Moiré pattern and doing the inverse Fourier transform, the beat component is clearly seen. The DFT-simulated STM image for the hydrogen-passivated armchair edge in Fig. 3*B* agrees excellently with the experimental result (Fig. 3*A*). We have also simulated the armchair edge with pentagons (15) and demonstrated that the atomic-scale node-like structure in the *y*-axis direction also occurs, as shown in Fig. 3*C*. These are contrasted to the case of the zigzag edge in Fig. 3*D* where no node-like structure but a periodic modulation is observed.

Next, we move on to scattering properties of graphene with superperiodic edge structures with atomic-scale defects in Fig. 4. In reality, graphene usually has such complex edge structures. The superperiodic armchair edges have no other propagating backscattering channels than the original intervalley and intravalley ones, if the radius of the Fermi surface is sufficiently small. Because the length of $G_{\parallel}$ in the superperiodic armchair structure is $\frac{1}{n}\times\frac{2\pi}{\sqrt{3}a}\approx\frac{1.47}{n}$ ($Å^{-1}$), where n is the multiple of the period, there can be other propagating backscattering channels for large n satisfying $n>\frac{1.47}{k_R}$. However, the reflection via those channels is quite small so long as the density of defects is low, and when $n<10$, it is sufficient to consider only two original scattering channels. A double-vacancy case and a single-adatom case for different supercell periods are considered. The solid (dashed) lines in Fig. 4 *A* and *B* are reflection probabilities of the armchair edge with relatively high (low) defect density, and the reflection probability is expected to approach asymptotically to the perfect armchair case in the low density defect limit. The overall shape of the reflection probability is quite insensitive to the hopping parameters of edge sites and the incident energy.

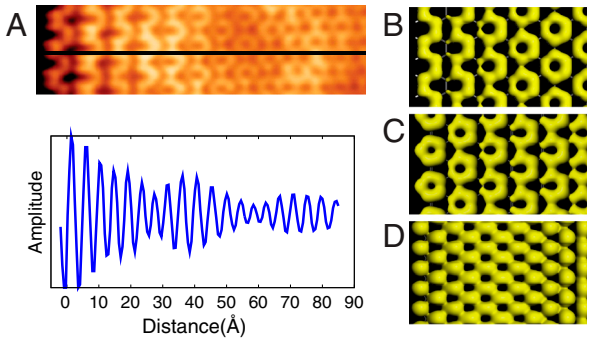

Fig. 3. (*A*) 6.0 nm × 1.5 nm STM topographic image (sample voltage bias −0.1 V and the tunneling current 0.5 nA) of the graphene armchair edge and its Fourier-filtered profile along the black straight line in the image. For comparison, DFT-simulated STM images are shown for (*B*) the armchair edge with hydrogen passivation, (*C*) the armchair edge with pentagons, and (*D*) the zigzag edge with hydrogen passivation, respectively.

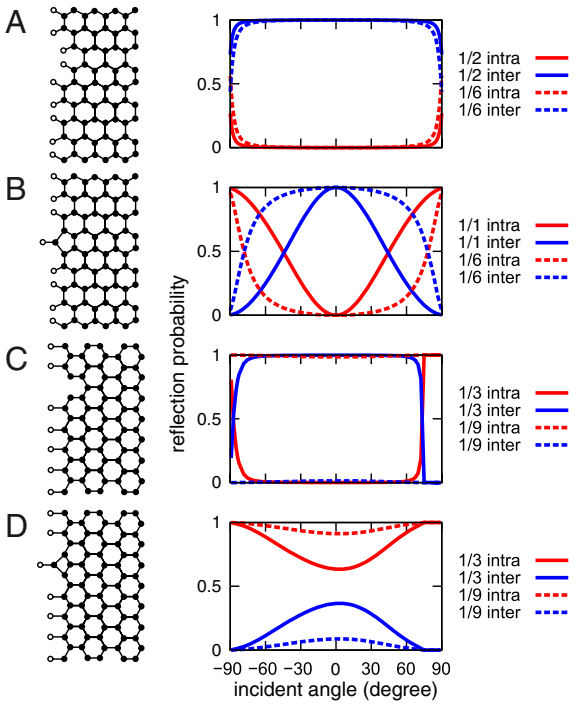

Fig. 4. Reflection probabilities of the K-valley-polarized wave of (*A*) double vacancies at the armchair edge, (*B*) adatoms at the armchair edge, (*C*) single vacancies at the zigzag edge, and (*D*) adatoms at the zigzag edge, respectively. Fractional numbers indicate the number of defects per unitcell along the edge.

For the superperiodic zigzag edge with defects, the intervalley scattering channel is open when the period is a multiple of three, because both K and K' fall on the Γ-point in the folded Brillouin zone. Therefore, both of intervalley and intravalley scatterings are allowed for the $3m$ (m: an integer) period while the only scattering channel at the $(3m+1)$ or $(3m+2)$ period edges is the intravalley one. Therefore, we show only the results of $3m$ period edges in Fig. 4 *C* and *D*. For vacancies introduced at the zigzag edge in Fig. 4*C*, the actual scattering channels change drastically depending on the period of the edge. The intervalley scattering becomes dominant at the $3m$ period edges while only intravalley scattering is allowed at other edges. If a carbon atom is attached to the zigzag edge as shown in Fig. 4*D*, the scattering becomes rather complicated. Although the reflection probability converges to the perfect zigzag edge limit at a low density of adatoms, a high density of adatoms makes the reflection probability strongly depend on hopping parameters and the incident electron energy. There is a clear asymmetry in reflection coefficients between positive and negative angles in Fig. 4 *C* and *D*, and an abrupt suppression of one channel around the incident angle of 90° occurs. These two features are due to the asymmetric trigonal warping (20) between K and K' valleys (see *SI Text*) and this asymmetry is reversed for the incident wave from the other (K') valley. As a result, only the intravalley scattering channel available (21) for a certain k_y range for the zigzag edge and that property was exploited for generating valley-polarized currents in the former theoretical work (22). Such an asymmetry is negligible at the armchair edge because of the mirror-symmetric pattern of trigonal warping with respect to the k_y-axis. More detailed analysis and understanding of the scattering at realistic edges with defects certainly require enormously more work in the future.

In summary, we have presented how the contributions from two valleys vary in the scattering at different graphene edges. For the zigzag edge, only intravalley scattering is possible due to the different edge-direction crystal momentum of two valleys, and a long-period decaying standing wave occurs as in conventional metals. The pseudospin changes its orientation in this case. For the armchair edge, in contrast, the wave is reflected mostly via intervalley scattering and the pseudospin is conserved. As a result, an atomic-scale node-like pattern and beats in the standing wave are generated near the edge. When the incident angle is small, this intervalley scattering process is quite robust in the presence of defects so that we can still observe nodal patterns even for edges of relatively high defect densities.

Materials and Methods

Theory. We used the density-functional theory (DFT) (23, 24) calculations and the tight-binding methods to obtain the simulated real-space STM images and reflection probabilities at graphene edges, respectively. The Perdew-Burke-Ernzerhof functional form (25) was adopted in the generalized gradient approximation and the ionic potentials were described by projector-augmented waves (26) implemented in the Vienna Ab initio Simulation Package (27). The plane wave basis with the kinetic energy cutoff of 300 eV was employed for describing wavefunctions, and the models were relaxed until the force on each atom was within 0.02 eV/Å. Tight-binding parameters were obtained from maximally localized Wannier function analysis using the Wannier90 package (28).

Experiment. Graphene was grown epitaxially on the silicon face of a highly *n*-doped 6H-SiC(0001) by thermal desorption of silicon at high temperature. To obtain high quality graphene and its edge structure, the pressure during the thermal desorption was kept below 3×10^{-9} Torr. The STM images were obtained at 300 K in ultrahigh-vacuum with an Omicron instrument. To filter out other effects such as the substrate structure and the graphene honeycomb lattice structure coexisting in the STM image, we used the WSxM software.

ACKNOWLEDGMENTS. We thank the Core Competence Enhancement Program (2E21580) of Korea Institute of Science and Technology (KIST) through the Hybrid Computational Science Laboratory and the Korean Government Ministry of Education, Science and Technology (MEST) Basic Research Grant No. KRF-2006-341-C000015 (C.P. and J.I.), Grant No. 2010-0007805 (G.K.) and the Priority Research Center Program (2010-0020207) (G.K.). Computations were performed through the support of Korea Institute of Science and Technology Information (KISTI).

1. Katsnelson MI, Novoselov KS, Geim AK (2006) Chiral tunnelling and the Klein paradox in graphene. *Nat Phys* 2:620–625.
2. Young AF, Kim P (2009) Quantum interference and Klein tunnelling in graphene heterojunctions. *Nat Phys* 5:222–226.
3. Cheianov VV, Fal'ko V, Altshuler BL (2007) The focusing of electron flow and a Veselago lens in graphene p-n junctions. *Science* 315:1252–1255.
4. Rycerz A, Tworzydło J, Beenakker CWJ (2007) Valley filter and valley valve in graphene. *Nat Phys* 3:172–175.
5. Nakada K, Fujita M, Dresselhaus G, Dresselhaus MS (1996) Edge state in graphene ribbons: nanometer size effect and edge shape dependence. *Phys Rev B* 54:17954–17961.
6. Kobayashi Y, Fukui KI, Enoki T, Kusakabe K (2006) Edge state on hydrogen-terminated graphite edges investigated by scanning tunneling microscopy. *Phys Rev B* 73:125415.
7. Girit ÇÖ, et al. (2009) Graphene at the edge: stability and dynamics. *Science* 323:1705–1708.
8. Huang H, Chen W, Chen S, Wee ATS (2008) Bottom-up growth of epitaxial graphene on 6H-SiC(0001). *ACS Nano* 2:2513–2518.
9. Son YW, Cohen ML, Louie SG (2006) Energy gaps in graphene nanoribbons. *Phys Rev Lett* 97:216803.
10. Yang H, et al. (2010) Quantum interference channeling at graphene edges. *Nano Lett* 10:943–947.
11. Crommie MF, Lutz CP, Eigier DM (1993) Imaging standing waves in a two-dimensional electron gas. *Nature* 363:524–527.
12. Everson MP, Jaklevic RC, Shen W (1990) Measurement of the local density of states on a metal surface: scanning tunneling spectroscopic imaging of Au(111). *J Vac Sci Technol* 8:3662–3665.
13. Hasegawa Y, Avouris Ph (1993) Direct observation of standing wave formation at surface steps using scanning tunneling spectroscopy. *Phys Rev Lett* 71:1071–1074.
14. Sasaki KI, Wakabayashi K (2010) Chiral gauge theory for the graphene edge. *Phys Rev B* 82:035421.
15. Koskinen P, Malola S, Häkkinen H (2009) Evidence for graphene edges beyond zigzag and armchair. *Phys Rev B* 80:073401.
16. Kim S, Ihm J, Choi HJ, Son YW (2008) Origin of anomalous electronic structures of epitaxial graphene on silicon carbide. *Phys Rev Lett* 100:176802.
17. Sakai KI, Takai K, Fukui KI, Nakanishi T, Enoki T (2010) Honeycomb superperiodic pattern and its fine structure near the armchair edge of graphene observed by low-temperature scanning tunneling microscopy. *Phys Rev B* 81 235417.
18. Sasaki K, Wakabayashi K, Enoki T (2011) Electron wave function in armchair graphene nanoribbons. *J Phy Soc Jpn* 80:044710.
19. Simon L, et al. (2009) Symmetry of standing waves generated by a point defect in epitaxial graphene. *Eur Phys J B* 69:351–355.
20. Castro Neto AH, Guinea F, Peres NMR, Novoselov KS, Geim AK (2009) The electronic properties of graphene. *Rev Mod Phys* 81:109–162.
21. McCann E, et al. (2006) Weak-localization magnetoresistance and valley symmetry in graphene. *Phys Rev Lett* 97:146805.
22. Pereira JM, Jr, Peeters FM, Costa Filho RN, Farias GA (2009) Valley polarization due to trigonal warping on tunneling electrons in graphene. *J Phys Cond Matt* 21:045301.
23. Kohn W, Sham L (1965) Self-consistent equations including exchange and correlation effects. *Phys Rev* 140:A1133.
24. Hohenberg P, Kohn W (1964) Inhomogeneous electron gas. *Phys Rev B* 136:B864.
25. Perdew JP, Burke K, Ernzerhof M (1996) Generalized gradient approximation made simple. *Phys Rev Lett* 77:3865–3868.
26. Kresse G, Joubert D (1999) From ultrasoft pseudopotentials to the projector augmented-wave method. *Phys Rev B* 59:1758–1775.
27. Kresse G, Furthmüller J (1996) Efficiency of ab-initio total energy calculations for metals and semiconductors using a plane-wave basis set. *Comput Mater Sci* 6:15–50.
28. Mostofi AA, et al. (2008) Wannier90: a tool for obtaining maximally-localized Wannier functions. *Computer Physics Communications* 178:685–699.

Supporting Information

Park et al. 10.1073/pnas.1114548108

SI Text

Tight-Binding Parameters from First-Principles Maximally Localized Wannier Functions. From the first-principles band calculation of uniformly sampled k-points [Monkhorst-Pack scheme (1)], we get diagonal $H(\mathbf{k})$ with the basis of Bloch eigenstates. Then, $H(\mathbf{k})$ can be Fourier transformed to the maximally localized Wannier function (MLWF) basis hamiltonian $H_{mn}(\mathbf{R})$ (2, 3). Here, m or n denotes the disentangled π-orbital induced band index and $\mathbf{R}$ is the lattice vector. These matrix elements decay rapidly as the distance between two MLWF becomes large. For ideal graphene, the nearest-neighbor hopping parameter extracted from this procedure is −2.88 eV and the next nearest- and 3rd nearest-neighbor ones are −0.24 eV and −0.26 eV, respectively. When edges are introduced, the hopping parameters are modified but rapidly converged to ideal graphene values within two or three sites away from the edge. The hopping parameters of three different armchair edges considered in the text are summarized in Fig. S1. These parameters are also used for the superperiodic graphene edge. Because the MLWF of the dangling armchair edge site is found to be the linear combination of the π- and σ-like orbitals of equal weight, we apply a unitary transformation to the $H_{mn}(\mathbf{R})$ and extract the hopping parameters of the effective π-like orbital decoupled from the σ-like orbital.

Method of Tight-Binding Boundary Matching. In the nearest-neighbor tight-binding model, the scattering wave in the bulk region can be expressed as a linear combination of the incident wave with the bulk Bloch states of the same energy. If the edge has a translational symmetry, backscattering states are limited to the ones that have the same crystal momentum component in the edge direction as the incident wave. If the edge direction is set to the y-axis, scattering waves in the bulk region ψ_G and the edge region ψ_S can be written as follows.

$$\psi_G = \psi^{\text{in}}(k_x,k_y) + \sum_{x'} r_i \psi^{\text{out}}(k_{x'},k_y), \qquad \text{[S1]}$$

$$\psi_S = \sum_i c_i G^i(E,k_y), \qquad \text{[S2]}$$

$$G^i(E,k_y) = (E - H_s(k_y))^{-1}|i\rangle. \qquad \text{[S3]}$$

Here, i is the index of the boundary site between the bulk and the edge regions and r_i and c_i are expansion coefficients for ψ_G and ψ_S, respectively. $k_{x'}$ can be evaluated from $\det(E - H(k_{x'},k_y)) = 0$ for given E and k_y, and is generally a complex number. The imaginary part of the wavevector reflects the decay length of each evanescent mode. The following two equations should be satisfied for all boundary sites.

$$\langle i|\psi_G\rangle = \langle i|\psi_S\rangle, \qquad \text{[S4]}$$

$$\langle i|E - (H_G + H_S - H_{DC})|\psi_G + \psi_S - \psi_{DC}\rangle = 0. \qquad \text{[S5]}$$

Eq. **S4** corresponds to the wavefunction matching at the boundary sites and Eq. **S5** ensures the stationary solution. By construction of Eqs. **S1** and **S2**, the stationary condition is automatically satisfied everywhere except for boundary sites so that we have only to consider the boundary sites.

The total Hamiltonian is written as the sum of three terms, H_G, H_S, and H_{DC}. H_G and H_S include the boundary site, and H_{DC} accounts for the double counting of boundary sites. Eq. **S5** can be rewritten as

$$\langle i|(-H_G + H_{DC})|\psi_G\rangle + c_i = 0. \qquad \text{[S6]}$$

Because the number of unknowns (r_i,c_i) is the same as the number of matching equations, we can uniquely determine the probabilities of all reflection modes. Then, the physically meaningful reflection probability R_i is determined from $r_i \cdot |\vec{V}_{\text{out}}|/|\vec{V}_{\text{in}}|$, where $\vec{V}_{\text{in}}$ and $\vec{V}_{\text{out}}$ are group velocities of the incident and scattered waves, respectively.

Analytic Solutions with Boundary Conditions. When the incident electron energy is small compared to the hopping parameters, we can get simple expressions for reflection coefficients of various armchair edges. For simplicity, the hopping parameter t is assumed to be all the same in the armchair edge with hydrogen passivation or pentagons. We start with the armchair edge without passivation. To investigate the effect of the increased hopping parameter at the edge, another hopping parameter t' is applied. (The hydrogen-passivated one can be automatically obtained from this case by setting $t' = t$.) Because there are two scattering channels in the armchair edge, the resulting K-valley scattering wave can be written as

$$\psi = \psi_K^{\text{in}} + r_{\text{intra}}\psi_K^{\text{out}} + r_{\text{inter}}\psi_{K'}^{\text{out}}. \qquad \text{[S7]}$$

The Bloch wavefunctions can be written as appropriate two-component pseudospin forms and we explicitly write the results for the conduction band of each valley as follows.

$$\psi_K = \frac{1}{\sqrt{2}}\begin{pmatrix} \exp\left(\frac{i\theta}{2}\right) \\ -\exp\left(-\frac{i\theta}{2}\right)\end{pmatrix}, \qquad \psi_{K'} = \frac{1}{\sqrt{2}}\begin{pmatrix} \exp\left(-\frac{i\theta}{2}\right) \\ \exp\left(\frac{i\theta}{2}\right)\end{pmatrix}, \qquad \text{[S8]}$$

where θ is the incident angle.

For small incident energy E, the coefficients of the K-valley incident wave are

$$\psi_K^{\text{in}}(\mathbf{C}1) = \exp\left(\frac{i\theta}{2}\right), \qquad \psi_K^{\text{in}}(\mathbf{C}2) = -\exp\left(-\frac{i\theta}{2}\right)\exp\left(\frac{2\pi i}{3}\right),$$
$$\psi_K^{\text{in}}(\mathbf{C}3) = -\exp\left(-\frac{i\theta}{2}\right), \qquad \psi_K^{\text{in}}(\mathbf{C}4) = \exp\left(\frac{i\theta}{2}\right)\exp\left(\frac{2\pi i}{3}\right), \qquad \text{[S9]}$$

and the coefficients of ψ_K^{out} can be obtained by substituting θ with $\pi - \theta$. When pseudospin components are replaced by K' values, K'-valley wavefunctions are also obtained. In the low-energy approximation, the stationary condition, $[E - H(k_y)]|\psi\rangle \approx -H(0)|\psi\rangle = 0$ $(E \approx 0, k_y \approx 0)$, is applied to the boundary **C**1 and **C**3 sites in Fig. S1, the scattering (reflection) coefficients r_{intra} and r_{inter} can be uniquely determined as follows:

$$r_{\text{intra}} = 0, \qquad r_{\text{inter}} = i\frac{t\exp(\frac{2\pi i}{3}) + t'}{t\exp(-\frac{2\pi i}{3}) + t'}. \qquad \text{[S10]}$$

In the low-energy approximation, the armchair edges with and without hydrogen passivation show a totally intervalley scattering.

The deviation from the numerical result in Fig. 2*B* of the text is due to the approximation of $H(k_y) \approx H(0)$.

The armchair edge with pentagons has the scattering site **C**1 in Fig. S1 and we should match the bulk and the edge wavefunctions by Eqs. **S4** and **S5**. Intra- and intervalley reflection coefficients are

$$r_{\text{intra}} = -\frac{\sqrt{3}\sin\theta}{\sqrt{3}+i\cos\theta}, \qquad r_{\text{inter}} = \frac{(2+2\sqrt{3}i)\cos\theta}{(\sqrt{3}-3i)+(\sqrt{3}+i)\cos\theta}, \qquad \textbf{[S11]}$$

and the reflection probabilities are

$$R_{\text{intra}} = \frac{3\sin^2\theta}{3+\cos^2\theta}, \qquad R_{\text{inter}} = \frac{4\cos^2\theta}{3+\cos^2\theta}. \qquad \textbf{[S12]}$$

In Fig. 2*C* of the text, we use the first-principles hopping parameters for a realistic simulation and the numerical result is only slightly different from this analytic result.

Trigonal Warping of the Fermi Surface. In the nearest-neighbor tight-binding description of graphene, the electronic energy spectrum of graphene around the Dirac point is given by (4)

$$E_{\pm}(\mathbf{q}) \approx \pm\frac{3ta}{2}|\mathbf{q}| \mp \frac{3ta^2}{8}\sin 3\theta_{\mathbf{q}}|\mathbf{q}|^2, \qquad \theta_{\mathbf{q}} = \tan^{-1}\frac{q_x}{q_y}, \qquad \textbf{[S13]}$$

where t is the nearest-neighbor hopping parameter, a the lattice constant of graphene, and $\mathbf{q}$ is the wavevector measured relative to the Dirac point. The threefold symmetric (trigonal) square term of $\mathbf{q}$ makes the Fermi surface deviate from a perfect circle as $|\mathbf{q}|$ increases. The trigonal warping direction is different for each valley and compared in Fig. S2.

From the crystal momentum conservation (or the translational symmetry) along the edge, the scattered wave should have the same k_y-component as the incident wave. In Fig. S2*A*, all incident waves in one valley have their own intervalley scattering pairs in the armchair edge. When $|k_y|$ is large, however, there can be no intervalley scattering pair in the zigzag edge owing to the warping direction as shown in Fig. S2*B*. We can show that this missing intervalley channel becomes slowly decaying evanescent one when $|k_y|$ of one valley exceeds the maximum $|k_y|$ of another valley. While there occur abrupt suppressions of intervalley channels due to this mismatch, scattering waves in real space are not so drastically changed near the edge because of the appearance of this evanescent wave.

Fourier Filtering of a Topographic Image. To validate our Fourier transform (FT) analysis, we show the original image of the regular armchair edge and the corresponding Fourier filtered image. Fig. S3*A* is the raw image without any image process. Atomic corrugations and other periodic structures are visible. Fig. S3*B* is the profile along the black line in Fig. S3*A*. It is clearly shown that a long wavelength pattern is mixed with short wavelength oscillations. The long wavelength $6\sqrt{3}\times 6\sqrt{3}R30°$ pattern is originated from the interaction between graphene and SiC substrate, and the short wavelength pattern can be explained by a mixture of short wavelength intervalley scattering and atomic corrugation. In this original image, however, the decay length and the long wavelength scattering are hard to analyze. This problem can be solved by the image processing, Fourier filtering. In Fig. S3*C*, we remove the image component of the $6\sqrt{3}\times 6\sqrt{3}R30°$ structure. The profile of this new image is shown in Fig. S3*D*. The former long wavelength oscillation disappeared. We do not lose any information about the behavior of the short wavelength oscillation by this filtering. This way, we can study only the component of the short wavelength oscillation, which is considered as a sign of intervalley scattering.

1. Monkhorst HJ, Pack JD (1976) Special points for Brillouin-zone integrations. *Phys Rev B* 13:5188–5192.
2. Marzari N, Vanderbilt D (1997) Maximally localized generalized Wannier functions for composite energy bands. *Phys Rev B* 56:12847–12865.
3. Souza I, Marzari N, Vanderbilt D (2001) Maximally localized Wannier functions for entangled energy bands. *Phys Rev B* 65:035109.
4. Castro Neto AH, Guinea F, Peres NMR, Novoselov KS, Geim AK (2009) The electronic properties of graphene. *Rev Mod Phys* 81:109–162.

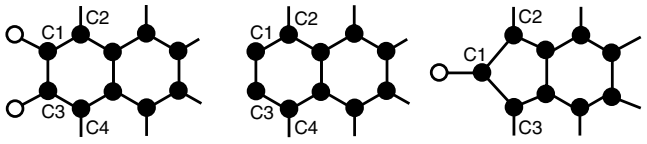

passivation (eV)		no passivation (eV)		pentagon (eV)	
C1 - C2	-2.92	C1 - C2	-3.03	C1 - C2	-2.25
C1 - C3	-2.85	C1 - C3	-3.78	C2 - C3	-1.84
C1 onsite	0.10	C1 onsite	0.49	C1 onsite	-0.02
C2 onsite	0.08	C2 onsite	-0.18	C2 onsite	0.11

Fig. S1. Hopping parameters from MLWF analysis. The onsite and nearest-neighbor hopping parameters of armchair edge with hydrogen passivation, without passivation, and with pentagons from the first-principles MLWF analysis. In ideal graphene, the nearest-neighbor hopping parameter is –2.88 eV.

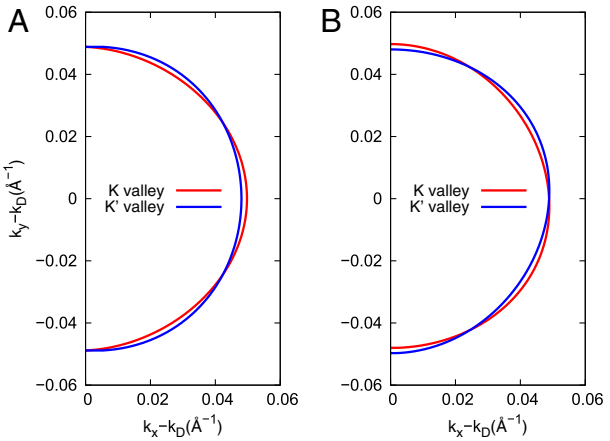

Fig. S2. Asymmetric trigonal warpings of Fermi surfaces around K and K' points. Fermi surfaces around K and K' points in the case of armchair edge (*A*) and zigzag edge (*B*) when $E_F - E_D = 0.3$ eV. For comparison, two Dirac points are shifted to the origin. k_D is the wavenumber representing the Dirac point in the Brillouin zone. The graphene edge is along the y-direction.

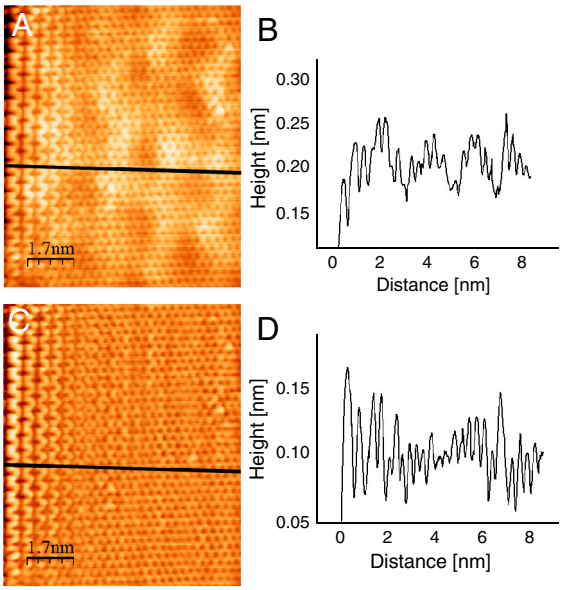

Fig. S3. 8 nm × 10 nm STM images of a regular armchair edge and corresponding profiles. (*A*) original image without any image process. The tunneling conditions were 50 mV, 0.5 nA. (*B*) Corresponding profile of (*A*). (*C*) Fourier filtered image from (*A*). The processing was done in WSxM software. We separated the image component of the interface structure between graphene and SiC. (*D*) corresponding profile of (*C*). Complicated short wavelength oscillations remained after the filtering.